Check for updates

Dissolvable templates to prepare Pt-based porous metallic glass for the oxygen reduction reaction†

Xiong Liang,‡[a] Zehang Liu,[a] Jianan Fu,[b] Heting Zhang,[a] Jinbiao Huang,[a] Shuai Ren,[a] Zhenxuan Zhang,[a] Qing Chen, [c] Yong Xiao,[d] Wenqing Ruan [*a] and Jiang Ma [*a]

Oxygen reduction reaction (ORR) plays a crucial role in electrochemical energy conversion and storage devices such as metal–air batteries and water electrolyzers. Herein, a hierarchical nanoporous platinum-based metallic glass (NPMG) was developed by a facile fabrication method by dissolving in a liquid. The surface topography of the sample can be easily modulated by controlling the particle size of sodium chloride. As a result, the NPMG was proved to be efficient and robust as the ORR catalysts with super hydrophilicity and self-renewal capacity. The half-wave potential of the platinum-based porous material was 835 mV at 0.1 M KOH, even higher than that of the commercial Pt/C catalyst (823 mV) and the previously reported platinum material. In particular, platinum-based porous materials have extremely long stability (more than 500 h) through the self-renewal surface, which perfectly meets the requirements of catalyst stability in batteries. Our study has a better inspiration for developing and applying novel catalysts to prepare metal–air batteries.

Introduction

With the growing global population and rapidly increasing energy demand, it is vital to develop efficient and eco-friendly energy conversion and storage systems. Among numerous electrochemical devices, metal–air batteries and water electrolyzers have been considered as promising technologies to meet future energy.[1–4] Oxygen reduction reaction (ORR) and oxygen evolution reaction (OER) are the two most important reactions in the above-mentioned energy conversion and storage devices. The sluggish kinetics of the ORR has long posed one of the biggest challenges in this field as the ORR is at the heart of the electrochemical conversion processes, and electrocatalysts are often required to improve the activity and durability of this reaction.[5] Thus, the ORR electrocatalyst properties dominate the related devices' overall performance and efficiency.[6–9] In the past few decades, the use of alloying,[10,11]

optimized coordination environments,[12] and surface strain[13–15] have resulted in platinum-based nanocrystals that enable high ORR activities. However, improving the stability of this catalyst remains challenging because of the poisoning of platinum.[16] It has been shown that catalytic activity, utilization, efficiency, and durability are improved by designing multicomponent catalytic surfaces.[17–19] Here, we show that the catalytic functionality and durability of nanostructured metallic glasses can be improved by morphological control.

As a new type of amorphous material, amorphous alloys, also known as metallic glasses (MGs), have received considerable attention since their discovery.[20–26] The unique disordered atomic stacking structure of MGs causes its viscosity to drop sharply in the supercooled liquid region (SLR), and this property enables it to behave like thermoplastic-formed (TPF)-like plastic under the synergistic effect of temperature and pressure.[27,28] Therefore, various micro/nanostructures can be prepared on the surface of MGs.[29,30] Moreover, owing to its amorphous nature, dealloying will occur when electrochemical experiments are performed,[31–33] thus exposing more active sites on the surface.[34] Numerous MGs formed on the micro/nanostructures by TPF have been reported, such as nanowires,[35] precision gratings,[36] and precision gears.[37] In contrast, due to the lack of templates and the difficulty in preparation, amorphous porous materials are rarely reported. The preparation of porous structures on MG is currently based on dealloying and pitting. However, these methods to prepare porous structures do not guarantee the original amorphous atomic structure, which hinders the unique excellent performance of

[a]Shenzhen Key Laboratory of High Performance Nontraditional Manufacturing, College of Mechatronics and Control Engineering, Shenzhen University, Shenzhen, 518060, China. E-mail: ruanwq@szu.edu.cn, majiang@szu.edu.cn
[b]Department of Mechanics and Aerospace Engineering, Southern University of Science and Technology, Shenzhen, 518055, China
[c]Department of Mechanical and Aerospace Engineering, The Hong Kong University of Science and Technology, Clear Water Bay, Kowloon, Hong Kong, China
[d]School of Materials Science and Engineering, Wuhan University of Technology, China

‡These authors contributed equally to this work.

MG. Owing to the amorphous nature of MG, dealloying will occur when an electrochemical experiment is performed, which will expose more active sites on the surface.[18,38,39] Bulk amorphous materials perfectly combine high macroscopic conductivity with surface active sites. Amorphism, credited to its high free energy, has recently been recognized as a contribution to ORR active sites.[40,41]

In this work, we developed a low-cost, controllable, and facile strategy for crafting large-area porous structures on MG surfaces by TPF *via* water-soluble salt as a template. The size of the porous surface structure can be easily modulated from 5 μm to 100 μm by changing the salt particle size. The prepared porous sample has an electrochemically active surface area 63 times that of the flat sample. For the ORR test, the porous catalyst exhibited a more positive half-wave potential (0.835 V *vs.* reversible hydrogen electrode (RHE)) than that of the benchmark Pt/C catalyst (0.823 V *vs.* RHE) at 1600 rpm with a Tafel slope of 52.2 mV dec^{-1}. Moreover, the porous catalyst also delivered more than 500 hours with a current density of 4 mA cm^{-2} at 0.54 V *versus* RHE for ORR durability measurement, which is in excellent agreement with our expectations.

Results and discussion

Hierarchical NPMG electrocatalyst

Fig. 1a illustrates the basic principle of preparing the hierarchical NPMGs electrocatalyst. The polished amorphous alloy and the ground sodium chloride were stacked together. Then, the amorphous plate was heated to its supercooled liquid zone at 10^{-3} Pa in a custom-designed vacuum furnace. Subsequently, the viscous MG surface was filled with sodium chloride particles under a pressure of 10 kN, and the sodium chloride particles were dissolved in water at ambient temperature to obtain an amorphous alloy surface with a porous structure. A straightforward dissolution process in which the sodium chloride template on the surface was completely dissolved in a short time within 5 minutes. All of these show that the NPMG obtained by dissolvable templates strategy has the advantage of easy preparation and demolding during the process. Fig. 1b shows the XRD patterns of NPMGs, MG, and NaCl, indicating that the NPMGs are fully glassy, characterized by a broad hump around 42°. The glassy properties were also determined using high-resolution transmission electron microscopy (TEM)
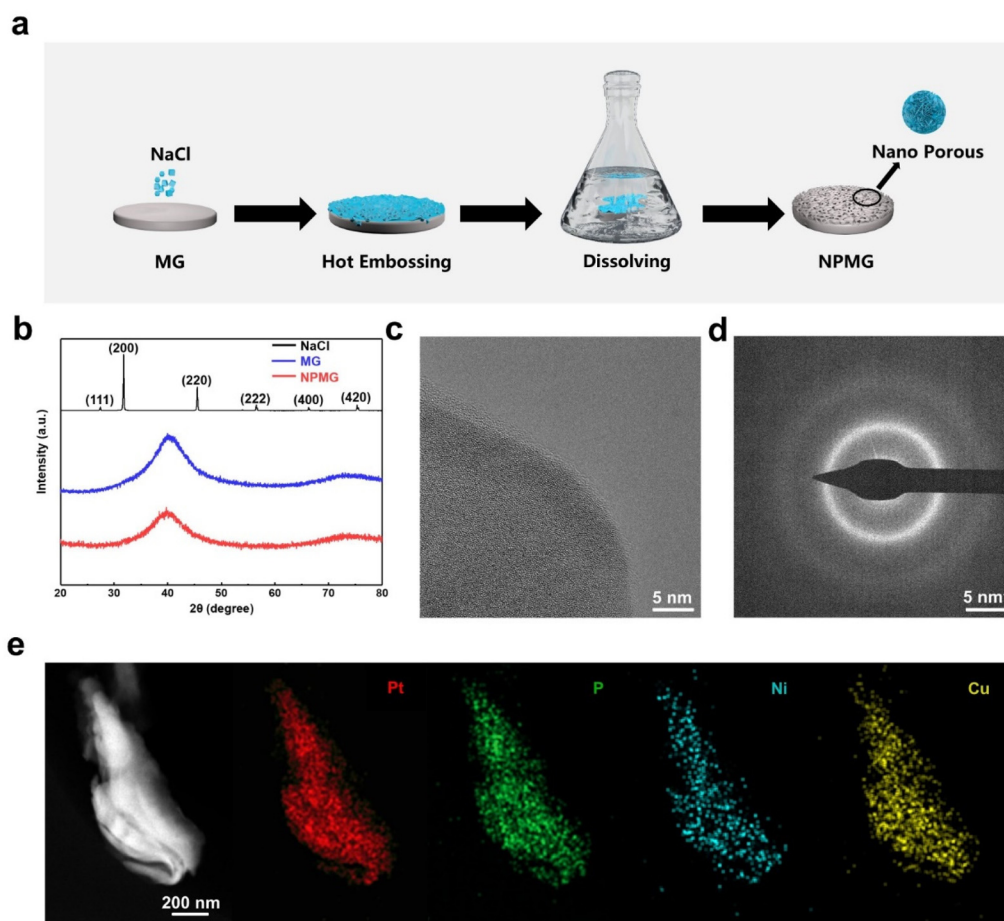

Fig. 1 (a) Fabrication of the hybrid electrocatalyst for the ORR; (b) the XRD patterns of NPMG, MG, and NaCl; (c) HAADF image showing the atomic structure of platinum-based amorphous NPMG; (d) the selected area electron diffraction pattern; (e) energy spectrum analysis shows the element distribution of the as-fabricated NPMG.

(shown in Fig. 1c), the disordered atomic structure indicates that the porous structure still has an amorphous nature, which was also confirmed by the diffraction rings in Fig. 1d. Fig. 1e displays the low-resolution TEM image and elemental mapping results of the porous structure. It can be seen that the elements Pt, Cu, Ni, and P are homogeneously distributed on the porous structure.

The reconstruction ability of the NPMGs with functional properties was also evaluated. When the structural properties of the material surface are changed or damaged, the entire porous structure on the MG surface was erased and the porous structure was prepared again by the same TPF process (Fig. S3†). The porous structure was constructed three times on the same MG through this cycle, and the XRD pattern (Fig. S4†) of the reconstructed samples exhibited typical amorphous peaks, demonstrating that NPMGs can be readily reconstructed even when the functional surface was destroyed, assuming an environment with sufficient space for material use.

The morphological characterization of NPMG

The development of advanced materials that can artificially regulate the size of the structure is a significant challenge. The microstructure of the NPMGs samples was characterized by scanning electron microscopy (SEM). Fig. 2a–c shows the image of porous with diameters of about 150 μm, 100 μm, and 5 μm, respectively. Large and tiny pores on the nano-thick flakes covered the MG surface, resulting in a hierarchical porous structure. Additionally, the size distribution of the irregular porous structure was determined from the SEM images ((Fig. S5†) and the average pore size matched the size of the salt particles used. It is worth noting that nanopores distributed on the nano-thick flakes will be found under SEM magnification, as shown in Fig. 2d–f. The average nanopore size of NPMG-5 μm is smaller than that in NPMG-100 μm (Fig. S6†), consistent with the BET test result that the specific surface areas of NPMG-5 μm, NPMG-100 μm, and NPMG-150 μm are 3.1729 m^2 g^{-1}, 1.1647 m^2 g^{-1}, and 0.807 m^2 g^{-1}, respectively (Fig. S7†). The presence of this pore structure increases the specific surface area of the porous MG, which will be beneficial to enhance the electrochemical properties of its surface. The size of the porous structure can be regulated by different sizes of salt particles, and the three-dimensional morphology of the porous structure (Fig. 2h–j) also further indicates the regulatability of the porous structure.

Electrocatalytic performance of the catalyst

To assess the ORR activity of NPMG at room temperature, a three-electrode system with a rotating disk electrode (RDE) was used in the O$_2$-saturated alkaline solution (0.1 M KOH). Linear sweep voltammetry (LSV) measurements were performed at different rotation rates to investigate the ORR kinetics in a
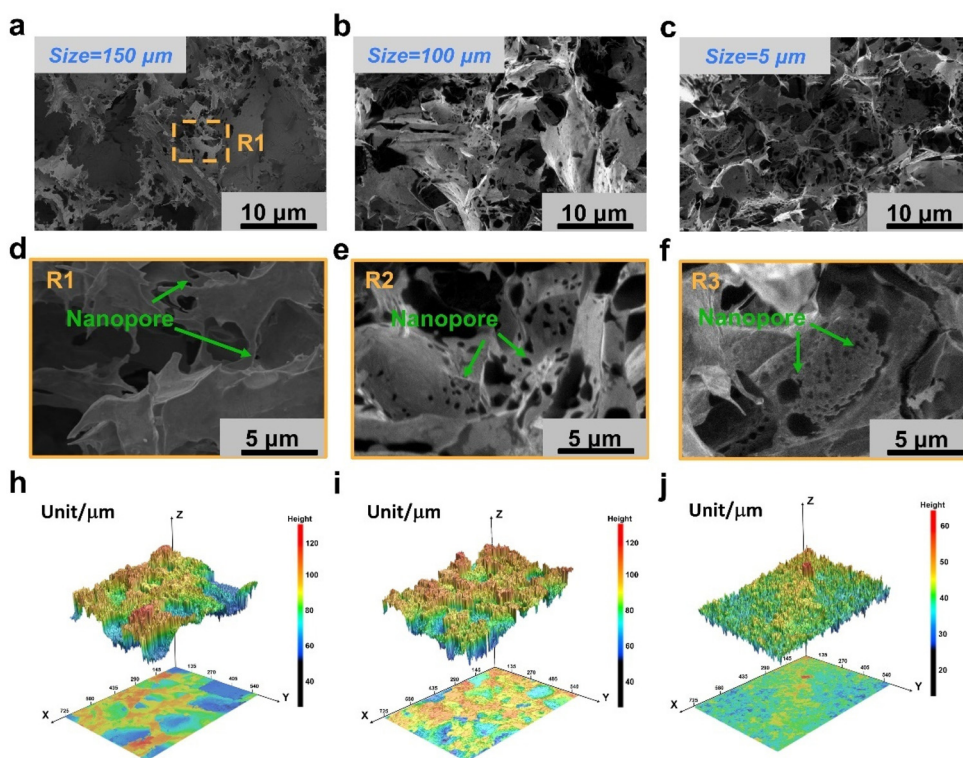

Fig. 2 (a)Porous morphology obtained using salt particles with a particle size of ~150 μm; (b) ~100 μm; (c) ~5 μm; (d) partial magnification image with a particle size of ~150 μm; (e) ~100 μm; (f) ~5 μm; (h) the three-dimensional porous morphology obtained using salt particles with a particle size of ~150 μm; (i) ~100 μm. (j) ~5 μm.

rotating disk electrode (RDE) configuration. Fig. 3a shows the LSV curves of two different sizes of NPMGs, MG plate and benchmark Pt/C (20 wt% Pt), where the current density is normalized to the geometric area. All the polarization curves with 90% resistance compensation were measured. At 1600 rpm, the NPMG-5 μm catalyst exhibited a more positive half-wave potential (835 mV *vs.* RHE) than that of the benchmark Pt/C

catalyst (823 mV *vs.* RHE), which indicates that the introduction of the porous structure is strong proof of enhanced ORR activity. ORR diffusion kinetics and electron transfer number (*n*) were investigated according to the Koutecky–Levich (K–L) eqn (Fig. 3b and d). The excellent ORR activity of the NPMG-5 μm catalyst was also substantiated by the smaller Tafel slope of 52.2 mV dec^{-1} than that of the benchmark Pt/C
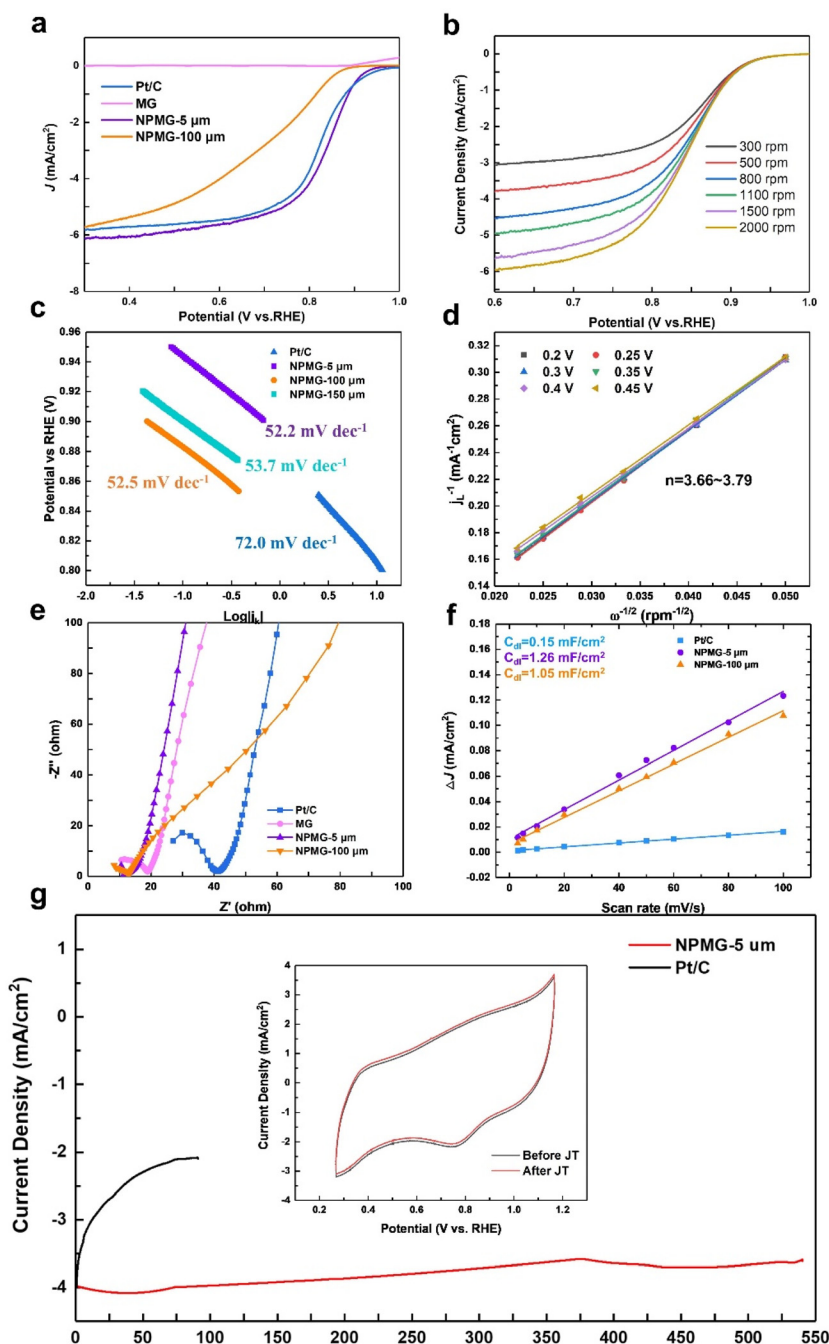

Fig. 3 (a) LSV curves of benchmark Pt/C, MG plate, and NPMGs; (b) LSV of NPMG-5 μm at different rotational speeds; (c) Tafel plot where the lines are fitting results; (d) Koutecky–Levich plot of J^{-1} *vs.* $\omega^{-1/2}$ at 0.20 V, 0.25 V, 0.30 V, 0.35 V, 0.40 V, and 0.45 V; (e) Nyquist plots of five samples from 1 00 000 kHz to 0.01 Hz for those samples; (f) a linear trend of Δ*J*/2 as a function of scan rate for those samples; (g) stability tests: *J*−*t* curve and CV curves before and after the long-term stability test (inset).

catalyst (72.0 mV dec^{-1}) (Fig. 3c). The Koutecky–Levich plots' linearity indicates first-order reaction kinetics concerning dissolved oxygen concentration and similar electron transfer numbers (n) at various potentials (Fig. 3d). The calculated n is in the range of 3.66–3.79 for the potential range of 0.20–0.45 V, demonstrating a four-electron ORR pathway over the NPMG-5 μm, similar to ORR catalyzed by the benchmark Pt/C catalyst under the same conditions.

As shown in Fig. 3e, electrochemical impedance spectroscopy (EIS) was used to provide high-frequency and low-frequency resistance to understand the catalytic performance further. The MG plate and NPMGs can show a simple equivalent circuit from the EIS diagram. It consists of a constant phase element (CPE), series resistance (R_S), and charge-transfer resistance (R_{ct}). NPMGs have a minor series resistance (R_S) than the MG plate and the benchmark Pt/C. Meanwhile, the semicircular diameter in the EIS spectrum of the NPMG catalyst is much smaller than that of the MG plate due to its smaller charge transfer resistance (R_{ct}), indicating a faster reaction rate and higher charge transfer efficiency.

Smaller NaCl template particle size contributes to the smaller porous size at each level of the NPMGs. Meanwhile, the charge transfer resistance is closely related to the synergistic effect of the porous structure and catalytic Pt active sites of NPMGs. By forming a hierarchical porous structure on the surface, more active sites are exposed, resulting in a decrease in the charge transfer resistance, which is also beneficial to the catalytic activity. We compared the SEM images of amorphous flat plates and NPMG and calculated the specific surface area, and the resulting nanopores have 63 times a more specific surface area than amorphous flat plates, and the active sites are closely related to the specific surface area.[42–44] For ORR, the protonation of O_2 to *OOH is the potential-determining step (PDS) at every active site in all models. The efficient active sites for ORR, ensure the superior catalytic ability.[45–47] The electrochemically active surface area (ECSA) of NPMGs was also estimated from the CV curve. As shown in Fig. 3f, a linear trend of $\Delta J/2$ as a function of scan rate was observed. The slope represents the geometric double-layer capacitance C_{dl}, which is linearly proportional to ECSA, therefore, the ratio between different catalysts can be used to evaluate ECSA. It is worth noting that the number of active sites on NPMG-5 μm was around eight times higher than that on Pt/C, indicating that the porous structure significantly increases active sites for the catalytic reaction.

To scrutinize the tolerance of the NPMG-5 μm and Pt/C catalysts to fuel the poisoning effect, a small amount of methanol was added to the electrolyte solution when running chronopotentiometry at 0.2 V (1600 rpm). When 50 mL methanol was added to 150 mL O_2-saturated 0.1 M KOH solution, no apparent change in current density was observed for the NPMG-5 μm catalyst, while a significant decrease in current density was seen for the Pt/C catalyst (Fig. S9†), revealing an excellent tolerance to methanol poisoning of NPMG-5 μm.
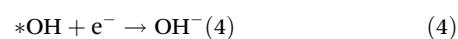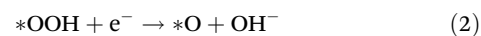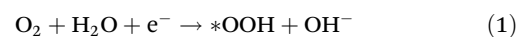
In addition to the catalytic activity, long-term stability is another critical concern of ORR catalysts, especially in commercial applications. The long-term stability of NPMG-5 μm was investigated at 0.40 V for 500 hours in an O_2-saturated 0.1 M KOH solution. As shown in Fig. 3g, the current is stable during the whole testing period without significant fluctuations, showing negligible deterioration. In sharp contrast with the Pt/C catalyst under the same condition, only ≈50% was retained after 100 hours. In addition, the CV test of NPMG-5 μm before and after 500 hours also demonstrates little loss in activity (Inset in Fig. 3g). To verify if the porous structure would disrupt during the ORR test in alkaline electrolyte, the SEM analysis was performed to detect the surface structure of the sample after a long-term stability test. It showed that the porous structure was basically unchanged as before (Fig. S10†).

Super hydrophilicity enhances the ORR activity

The surface structure of the catalyst will significantly affect the ORR properties.[4,8,9,39–41] To illustrate the structural origin of the high catalytic activity of NPMG-5 μm, contact angle (CA) tests of the MG plate and NPMG-5 μm were performed. As shown in Fig. 4a, the contact angle of the water drop (WCA) was 70° on the smooth surface of the MG plate. In contrast, the WCA was 8° on the surface of NPMG-5 μm. During the dynamic contact process, the water drop on NPMG-5 μm was wholly immersed into the surface with a CA close to 0° in a short time of fewer than 0.01 seconds, while the CA of the MG plate was still at 52° after 10 seconds. It shows that NPMG-5 μm has super hydrophilicity, which results in a more active ORR catalyst.[42,43] Fig. 4b summarizes the dynamic water contact performance for NPMG-5 μm and the MG plate. As shown in Fig. 4b, due to the super hydrophilicity of the NPMG-5 μm surface, it had a larger contact surface area with the electrolyte compared to the smooth and unstructured surface of the MG plate at the same size. It is well known that the adsorbed H_2O could serve as the reactive precursors and then play an important role in promoting the electrocatalytic kinetics during ORR in alkaline media.[40,48] The superior hydrophilic affinity as well as the strong metal-support effect would be very helpful for improving the adsorption behaviors of the reactive precursors, reducing the formation barrier of the intermediates and promoting the mass transportation of products during the catalytic process,[49–51] achieving a fast catalytic kinetics toward efficient ORR for catalysts. This made the water molecules in the electrolyte easier to come in contact with the active sites, thus significantly improving the reaction rate. In the ORR progress, The reaction steps are divided into four steps, and the four-electron transfer steps are as follows:

The reaction of four electron processes: $O_2 + 2H_2O + 4e^- = 4OH^-$,

$$O_2 + H_2O + e^- \rightarrow *OOH + OH^- \tag{1}$$

$$*OOH + e^- \rightarrow *O + OH^- \tag{2}$$

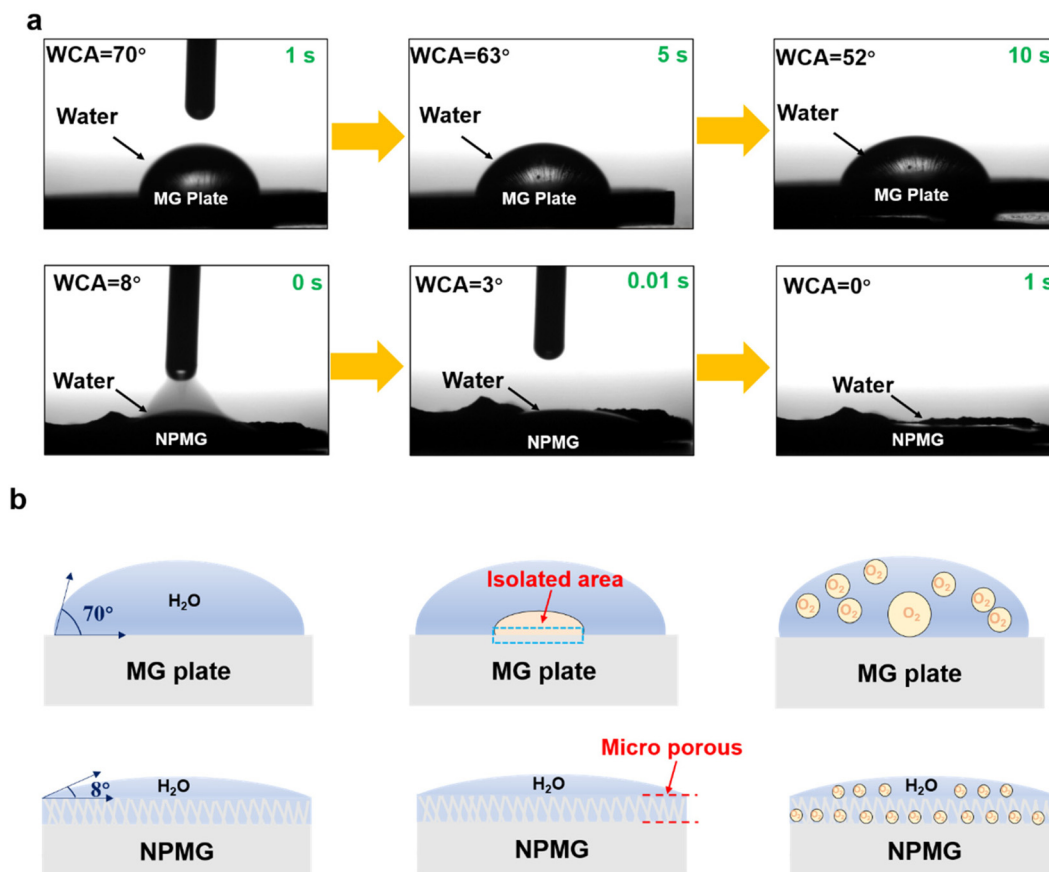$$*OH + e^- \rightarrow OH^- (4) \tag{4}$$

Fig. 4 (a) WAC of NPMG-5 μm and MG plate; (b) Sketch of the ORR on the surface of the MG plate and NPMG-5 μm.

the potential key reaction is the conversion of O* to OOH* in the third step.[52,49] The super hydrophilicity enables the OH^- in water to bind better to the active site, bringing new inspiration for preparing new oxygen reduction catalysts. Therefore, the super hydrophilic NPMG-5 μm provides more accessible channels for water molecules to react on active sites than the unstructured substrate, making it an efficient catalyst supporter for the ORR.

Element variation after ORR

Although the porous structure of NPMG-5 μm is basically unchanged after the long-term stability test, the surface's compositional structure and electronic state over the course of the dealloying process were investigated by X-ray photoelectron spectroscopy (XPS) (Fig. 5a–d). The Pt 4f spectra show a positive shift (+0.3 eV) of deconvoluted Pt^0, Pt^{2+} peaks that appeared from NPMG-5 μm after the long-term stability test. We find that the Pt^{2+} peaks increase in intensity with dealloying, and two peaks near 74.9 and 77.8 eV are increased after the long-term stability test, which corresponds to further oxidation to Pt^{4+}. The XPS spectra of Cu show that this element is removed from the NPMG-5 μm surface after the long-term stability test (Fig. 5b); however, the P remains on the surface

(Fig. 5c), and the Ni^0 on the surface was oxidized to Ni^{2+}(Fig. 5d).

The positive shift of Pt^0, Pt^{2+}, and Pt^{4+} peaks after the long-term stability test is therefore attributable to the decreased coordination with Cu, causing the outer shell Pt electrons to be more strongly bound to their nuclei. The NPMG-5 μm surface was continuously modified through the dealloying progress, which formed a porous interface enriched with Pt sites, agreeing with the higher ECSA values for NPMG-5 μm after the long-term stability test (Fig. S12†). Consistent with the result of the long-term stability test, the self-renewal capacity of the NPMG-5 μm suggested excellent long-term durability.

The half-wave potential, Tafel slope, and stability of NPMG-5 μm were compared with those of ORR electrocatalysts reported in the literature, including noble metals, single-atom catalysts, transition metal oxides, transition metal dichalcogenides, transition metal nitrides, transition metal phosphides, transition metal carbides, transition metal borides, metallic glasses, and metal-free catalysts (see Fig. 6 and Table S1†). It is encouraging to see that the performance of the NPMG-5 μm is superior to that of the most previously reported catalysts for the ORR in an alkaline solution. Both a low Tafel slope and a high stability
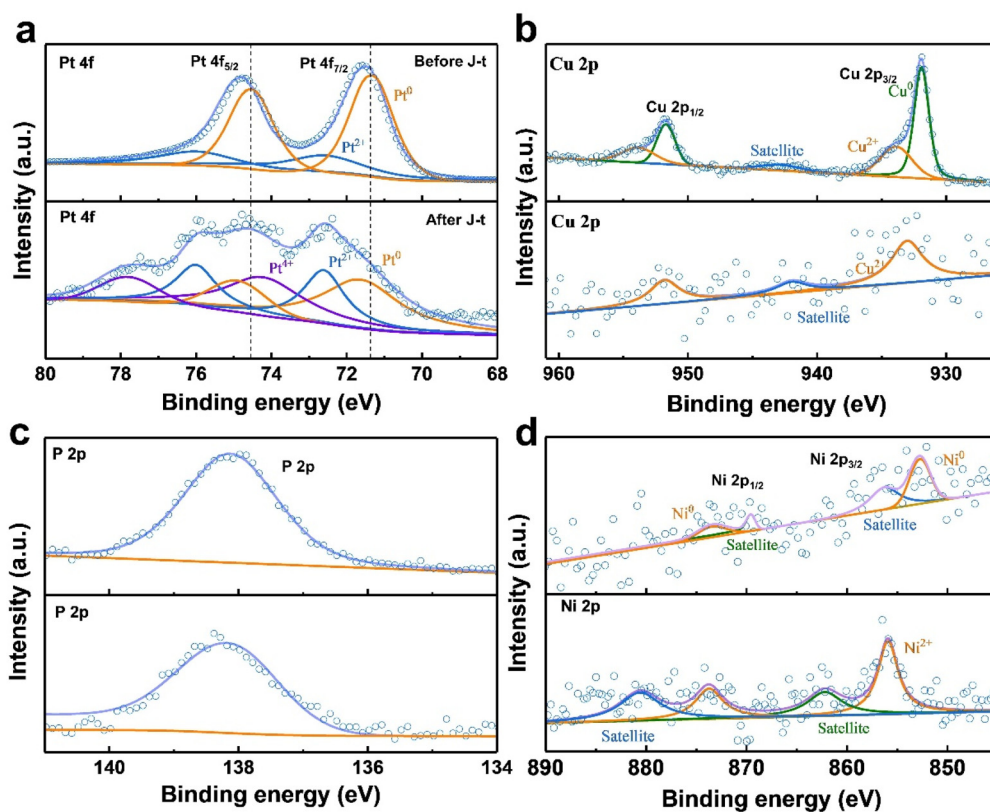
Fig. 5 Surface characterization of dealloyed NPMG: X-ray photoelectron spectra (XPS) for (a) Pt 4f; (b) Cu 2p; (c) P 2p; and (d) Ni 2p of NPMG.

time can be obtained with this catalyst. This work proposes a simple and universal strategy to synthesize MG catalysts. The hydrophilic and porous structure with a large specific area could significantly increase the activity. The dealloying of the glassy matrix leads to self-maintaining catalytic activity upon long-term usage.
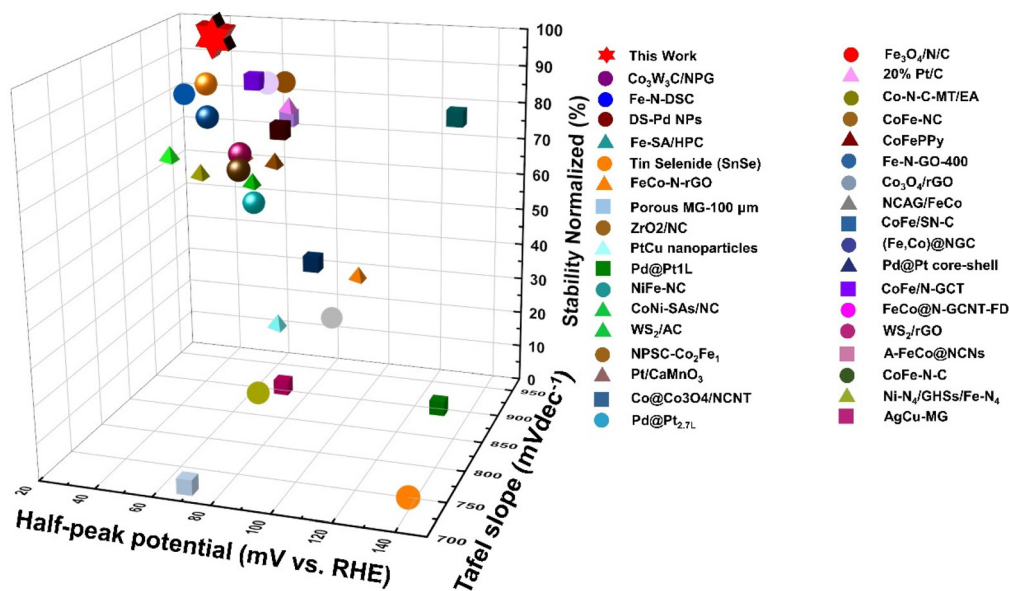

Fig. 6 Half-wave potential, Tafel slope, and stability comparisons of the ORR catalyst in the present work with different categories reported in previous literature. More details can be found in Table S1.†

Experimental step

Preparation of the MG

$Pt_{57.5}P_{22.5}Cu_{14.7}Ni_{5.3}$ as an amorphous alloy was studied as a component of catalytic materials, which has been demonstrated through several strategies of subtractive and additive surface modification on MG surfaces to form unique morphologies and compositions by post-processing.[53] The subtractive modification involved dealloying of non-functional components to enrich Pt-based MG surfaces with Pt and increase surface areas through pore formation.[54,55] The additive modification was accomplished with underpotential deposition,[56] galvanic displacement,[57] and electrodeposition[58] to introduce new species (Ru and MnO_x) to the MG surface[59,60]

The PtPCuNi bulk glassy alloy was selected in the present study because this has been proven to have good flow properties and to be thermally stable in its SLR, which meets the requirements for TPF (as shown in Fig. 1a). In addition, this composition has been demonstrated to be feasible for use as an ORR electrocatalyst in its ribbon form. Amorphous $Pt_{57.5}P_{22.5}Cu_{14.7}Ni_{5.3}$ rod with a diameter of 5 mm was obtained from Pt 57.5 at%, P 22.5 at%, Cu 14.7 at%, and Ni 5.3 at% by a conventional water-cooled copper manufacturing method. It is convenient to make it thermoformed by hot pressing. The rod was cut into disks with a thickness of 1 mm and then polished with abrasive paper and a polishing machine.

Details of NPMGs by TPF

Sodium chloride was used as a template to grind and adjust the pore size to adjust the size of the porous structure in the experiment. The sodium chloride template and the polished sample were stacked in order from top to bottom, and installed in a mold with a through-hole (a diameter of 7.5 mm) in the center. After that, the sample was hot-pressed in the mold under a pressure of 10 kN in a low vacuum environment of 195–205 °C and kept pressing for 15 seconds under this condition. After that, the pressure was removed. When the sample was cooled to room temperature, it was taken out of the mold and then placed in distilled water. The hot-pressed sample was soaked in the solution for 30 minutes to remove the residual sodium chloride template on the surface of the sample. The sodium chloride template was wholly dissolved in distilled water. The Pt-based MG with porous on its surface was obtained. The optical image of the surface of the Pt-based MG porous structure is shown in Fig. S1.†

Electrochemical measurement

The electrocatalytic activities towards the ORR were evaluated on an electrochemical workstation (CHI 660E, Chenhua, Shanghai, China) in a standard three-electrode mode with a PEM at room temperature. A platinum sheet was used as the counter electrode, and a silver chloride electrode was used as the reference electrode. All the electrochemical measurements were performed in 0.1 mol L^{-1} KOH. For comparison, the electrochemical performance of commercial 20 wt% Pt/C with a loading of 0.229 mg cm^{-2} was tested, which was prepared

with 15 μL ink (Pt/C 3 mg mL^{-1}) and loaded onto a clean glassy carbon electrode (GCE, 5 mm in diameter). The ORR activities were evaluated using LSV at 5 mV s^{-1}. The potential values reported in this study are *versus* the reversible hydrogen electrode (RHE) and are transformed to E *vs.* RHE using the equation E (*vs.* RHE) = E(AgCl) + 0.197 V. Tafel plots were fitted to the Tafel equation: $\eta = \beta \log j + \alpha$, where η is the half-wave potential, β is the Tafel slope, j is the current density, and α is the Tafel intercept relative to the exchange current density j. Cyclic voltammetry (CV) was carried out at various scan rates between 0.1 and 0.2 V *vs.* RHE to estimate the electrochemically active surface area (ECSA). Electrochemical impedance spectroscopy (EIS) was performed with frequencies ranging from 0.01 Hz to 10^6 Hz with an amplitude of 5 mV. Durability was measured by the following methods: chronoamperometry at 0.40 V.

Characterization of physical properties

The amorphous nature of the as-cast MG, NPMGs, and sodium chloride peak before template dissolution was ascertained by X-ray diffraction (XRD; Rigaku MiniFlex600) with Cu Kα radiation. The surface chemical state was analyzed by X-photoelectron spectroscopy (XPS, Thermo Scientific K-Alpha). All binding energies were at the carbon 1s position of the pollutant carbon in the vacuum chamber of the instrument (284.4 electron volts) calibration. An FEI Quanta 450 FEG scanning electron microscope instrument, JEOL 2100F scanning transmission electron microscope (STEM) equipped with a double spherical aberration corrector, and energy dispersive spectrometer (EDS) were used to characterize the morphology and element distribution of the samples. The contact angle (CA) of the microstructure surface was measured using a droplet shape analyzer (DSA100S, Krüss, Germany), and the volume of water droplets was 1 μL.

Conclusion

In conclusion, we developed a flexible and universal strategy to prepare efficient and robust porous metallic ORR catalysts. Through TPF, the surface of MG formed a hierarchical porous structure with a nanoscale pinpoint. By forming the hierarchical porous structure, NPMG-5 μm exhibits excellent catalytic performance, with a half-wave potential of 835 mV exceeding that of Pt/C. EIS measurement shows that the NPMG-5 μm has excellent charge transfer efficiency. The ECSA results showed that the number of active sites in NPMG-5 μm was more than eight times that in Pt/C catalysts. Astonishingly, the NPMG-5 μm catalyst is ultra-stable, exhibiting slight deterioration after the ORR for 500 hours. The super hydrophilicity and the self-renewal capacity of NPMG-5 μm are responsible for the outstanding ORR performance and originate from the surface structural construction. Our results provide a novel, universal method for designing superior ORR catalysts with excellent activity and stability.

Author contributions

Ruan W and Ma J conceived the idea. Liang X, Ren S, Zhang Z, Xiao Y, and Chen Q supervised the work. Liu Z and Fu J carried out the experiments, and Zhang H, and Huang J designed the experimental setup. Liu Z performed XRD and SEM. Fu J performed the raw material preparation. Liang X and Liu Z performed the TEM. Ruan W, Ma J, and Liu Z wrote the manuscript. All authors contributed to the discussion and analysis of the results.

Conflicts of interest

The authors declare no competing financial interests.

Acknowledgements

References

1 Z. Caia, P. Wanga, J. Yanga and X. Wanga, *Energy Environ.*, 2019, **5**, 22–36.

2 S. Gupta, W. Kellogg, H. Xu, X. Liu, J. Cho and G. Wu, *Chem. – Asian J.*, 2016, **11**, 10–21.

3 X. Lv, W. Tian, Y. Liu and Z.-Y. Yuan, *Chem. Front.*, 2019, **3**, 2428–2436.

4 M. A. Ahsan, T. He, K. Eid, A. M. Abdullah, M. F. Sanad, A. Aldalbahi, B. Alvarado-Tenorio, A. Du, A. R. P. Santiago and J. Noveron, *ACS Appl. Mater. Interfaces*, 2022, **14**, 3919–3929.

5 R. Hu, Y. Li, Q. Zeng and J. Shang, *Appl. Surf. Sci.*, 2020, **525**, 146588.

6 A. Kulkarni, S. Siahrostami, A. Patel and J. K. Nørskov, *Chem. Rev.*, 2018, **118**, 2302–2312.

7 X. F. Lu, B. Y. Xia, S. Q. Zang and X. W. Lou, *Angew. Chem.*, 2020, **132**, 4662–4678.

8 T. T. Cui, Y. P. Wang, T. Ye, J. Wu, Z. Q. Chen, J. Li, Y. P. Lei, D. S. Wang and Y. D. Li, *Chem., Int. Ed.*, 2022, **61**, e202115219.

9 L. H. Liang, H. H. Jin, H. Zhou, B. S. Liu, C. X. Hu, D. Chen, J. W. Zhu, Z. Wang, H. W. Li, S. L. Liu, D. P. He and S. C. Mu, *J. Energy Chem.*, 2022, **65**, 48–54.

10 J. K. Nørskov, T. Bligaard, J. Rossmeisl and C. H. Christensen, *Nat. Chem.*, 2009, **1**, 37–46.

11 V. R. Stamenkovic, D. Strmcnik, P. P. Lopes and N. M. Markovic, *Nat. Mater.*, 2017, **16**, 57–69.

12 M. Li, Z. Zhao, T. Cheng, A. Fortunelli, C.-Y. Chen, R. Yu, Q. Zhang, L. Gu, B. V. Merinov and Z. Lin, *Science*, 2016, **354**, 1414–1419.

13 M. Escudero-Escribano, P. Malacrida, M. H. Hansen, U. G. Vej-Hansen, A. Velázquez-Palenzuela, V. Tripkovic, J. Schiøtz, J. Rossmeisl, I. E. Stephens and I. Chorkendorff, *Science*, 2016, **352**, 73–76.

14 M. Luo and S. Guo, *Nat. Rev. Mater.*, 2017, **2**, 1–13.

15 I. E. L. Stephens, J. Rossmeisl and I. Chorkendorff, *Science*, 2016, **354**, 1378–1379.

16 Y. Yuan, J. Wang, S. Adimi, H. Shen, T. Thomas, R. Ma, J. P. Attfield and M. Yang, *Nat. Mater.*, 2020, **19**, 282–286.

17 Y. C. Hu, Y. Z. Wang, R. Su, C. R. Cao, F. Li, C. W. Sun, Y. Yang, P. F. Guan, D. W. Ding and Z. L. Wang, *Adv. Mater.*, 2016, **28**, 10293–10297.

18 F. Hu, S. Zhu, S. Chen, Y. Li, L. Ma, T. Wu, Y. Zhang, C. Wang, C. Liu, X. Yang, L. Song, X. Yang and Y. Xiong, *Adv. Mater.*, 2017, **29**, 1606570.

19 G. Doubek, R. C. Sekol, J. Li, W. H. Ryu, F. S. Gittleson, S. Nejati, E. Moy, C. Reid, M. Carmo and M. Linardi, *Adv. Mater.*, 2016, **28**, 1940–1949.

20 A. Inoue, B. Shen, H. Koshiba, H. Kato and A. R. Yavari, *Nat. Mater.*, 2003, **2**, 661–663.

21 W.-H. Wang, C. Dong and C. Shek, *Mater. Sci. Eng., R*, 2004, **44**, 45–89.

22 H. Guo, P. Yan, Y. Wang, J. Tan, Z. Zhang, M. Sui and E. Ma, *Nat. Mater.*, 2007, **6**, 735–739.

23 X. Liang, J. Ma, X. Wu, B. Xu, F. Gong, J. Lei, T. Peng and R. Cheng, *J. Mater. Sci. Technol.*, 2017, **33**, 703–707.

24 R. Vaidyanathan, M. Dao, G. Ravichandran and S. Suresh, *Acta Mater.*, 2001, **49**, 3781–3789.

25 H. L. Meng, S. Y. Lin, J. J. Feng, L. Zhang and A. J. Wang, *J. Colloid Interface Sci.*, 2022, **610**, 573–582.

26 J. Fu, J. Yang, K. Wu, H. Lin, W. Wen, W. Ruan, S. Ren, Z. Zhang, X. Liang and J. Ma, *Mater. Horiz.*, 2021, **8**, 1690–1699.

27 W. Wang, *Adv. Mater.*, 2009, **21**, 4524–4544.

28 M. Chen, *NPG Asia Mater.*, 2011, **3**, 82–90.

29 J. Ma, Z. Huang, H. Zheng, F. Gong and X. Liang, *Mater. Res. Exp.*, 2019, **6**, 075210.

30 J. Fu, Z. Li, Z. Liu, X. Li, W. Wen, F. Sun, L. Li, J. Huang, W. Ruan, S. Ren, Z. Zhang, X. Liang and J. Ma, *Sci. China Mater.*, 2022, **65**, 2833–2841.

31 Q. Jing, B. Zhang, J. Zhang, M. Z. Ma and R. P. Liu, *Sci. China: Phys., Mech. Astron.*, 2010, **53**, 2223–2226.

32 M. Guo, H. Wang, J. Liu and L. Ouyang, *J. Non-Cryst. Solids*, 2022, **588**, 121646.

33 J. Fu and J. Ma, *Adv. Eng. Mater.*, 2022, 2200659, DOI: **10.1002/adem.202200659**.

34 D. Duan, X. Yin, J. Zhao, S. Liu and Y. Wang, *Ionics*, 2022, **28**, 1377–1386.

35 J. Fu, Z. Huang, J. Yang, J. Ma and J. Shen, *J. Non-Cryst. Solids*, 2021, **558**, 120682.

36 H. Xu, F. Li, W. Zhao, S. Wang, Y. Du and C. Bian, *J. Sens.*, 2019, **2019**, 7.

37 J. Shaikh, N. K. Jain and V. Venkatesh, *Mater. Manuf. Processes*, 2013, **28**, 1117–1123.

38 J. Wu, H. Zhou, Q. Li, M. Chen, J. Wan, N. Zhang, L. Xiong, S. Li, B. Y. Xia, G. Feng, M. Liu and L. Huang, *Adv. Energy Mater.*, 2019, **9**, 1900149.

39 X. Liu, W. Zhang, X.-H. Liu, K. Li and X. Zhang, *J. Electroanal. Chem.*, 2022, **906**, 116023.

40 L. Liu, Z. Xu, L. Cao, Y. Jia, Z. Yao, Z. Xu, R. Li and Z. Zi, *Colloids Surf., A*, 2022, **646**, 128997.

41 K. Chu, X. Li, Y. Tian, Q. Li and Y. Guo, *Energy Environ. Mater.*, 2022, **5**, 1303–1309.

42 Y. Chen, S. Hu, F. Nichols, F. Bridges, S. Kan, T. He, Y. Zhang and S. Chen, *J. Mater. Chem. A*, 2020, **8**, 11649–11655.

43 H. Li, Y. Wen, M. Jiang, Y. Yao, H. Zhou, Z. Huang, J. Li, S. Jiao, Y. Kuang and S. Luo, *Adv. Funct. Mater.*, 2021, **31**, 2011289.

44 Y. Luo, J. Zhang, J. W. Chen, Y. H. Chen, C. Y. Zhang, Y. J. Luo, G. Wang and R. L. Wang, *J. Catal.*, 2021, **397**, 223–232.

45 J. Tang, C. Wang, H. Zhang and J. Guo, *J. Alloys Compd.*, 2022, **911**, 164991.

46 M. Wang, H. Zheng, Y. Dong, Z. Jin, S. Liao, W. Gong, X. Li, Z. Li, M. Xia and J. Wang, *Appl. Phys. Lett.*, 2022, **120**, 261903.

47 S. Wu, H. Liu, G. Lei, H. He, J. Wu, G. Zhang, F. Zhang, W. Peng, X. Fan and Y. Li, *Chem. Eng. J.*, 2022, **441**, 135849.

48 W. Cheng, X. Zhao, H. Su, F. Tang, W. Che, H. Zhang and Q. Liu, *Nat. Energy*, 2019, **4**, 115–122.

49 H. Su, W. Zhou, H. Zhang, W. Zhou, X. Zhao, Y. Li, M. Liu, W. Cheng and Q. Liu, *J. Am. Chem. Soc.*, 2020, **142**, 12306–12313.

50 X. Luo, X. Wei, H. Wang, W. Gu, T. Kaneko, Y. Yoshida, X. Zhao and C. Zhu, *Nano-Micro Lett.*, 2020, **12**, 163.

51 F. Tang, W. Cheng, Y. Huang, H. Su, T. Yao, Q. Liu, J. Liu, F. Hu, Y. Jiang, Z. Sun and S. Wei, *ACS Appl. Mater. Interfaces*, 2017, **9**, 26867–26873.

52 K. Dang, S. H. Zhang, X. W. Wang, W. M. Sun, L. G. Wang, Y. Tian and S. H. Zhan, *Nano Res.*, 2021, **14**, 4848–4856.

53 G. Doubek, R. C. Sekol, J. Li, W.-H. Ryu, F. S. Gittleson, S. Nejati, E. Moy, C. Reid, M. Carmo, M. Linardi, P. Bordeenithikasem, E. Kinser, Y. Liu, X. Tong, C. O. Osuji, J. Schroers, S. Mukherjee and A. D. Taylor, *Adv. Mater.*, 2016, **28**, 1940–1949.

54 B. Han, C. Carlton, A. Kongkanand, R. Kukreja, B. Theobald and L. Gan, *Energy Environ. Sci.*, 2015, **8**, 258–266.

55 Q. Chen and K. Sieradzki, *Nat. Mater.*, 2013, **12**, 1102–1106.

56 H. W. Pickering, *Corros. Sci.*, 1983, **23**, 1107–1120.

57 J. Erlebacher, M. J. Aziz, A. Karma, N. Dimitrov and K. Sieradzki, *Nature*, 2001, **410**, 450–453.

58 S. Ding, Y. Liu, Y. Li, Z. Liu, S. Sohn, F. J. Walker and J. Schroers, *Nat. Mater.*, 2014, **13**, 494–500.

59 J. Schroers, *Adv. Mater.*, 2010, **22**, 1566–1597.

60 R. C. Sekol, X. Li, P. Cohen, G. Doubek, M. Carmo and A. D. Taylor, *Appl. Catal., B*, 2013, **138–139**, 285–293.